DOI: 10.13009/EUCASS2022-4460
9TH EUROPEAN CONFERENCE FOR AERONAUTICS AND SPACE SCIENCES (EUCASS)

REST HF-10 test case: Large-Eddy Simulations using the AVBP solver

Thomas Schmitt[1†], *David Marchal*[1], *Sébastien Ducruix*[1], *Bénédicte Cuenot*[2]
[1]*Laboratoire EM2C, CNRS, CentraleSupélec, Université Paris-Saclay,*
3, rue Joliot Curie, 91192 Gif-sur-Yvette cedex, France
[2]*Centre Européen de Recherche et de Formation Avancée en Calcul Scientifique (CERFACS),*
42, Avenue Gaspard Coriolis, 31057 Toulouse Cedex 01, France
[†]Corresponding author (thomas.schmitt@centralesupelec.fr)

Abstract

The HF-10 test case, from the REST (Rocket Engine Stability Initiative) working group, is a typical injection element of LOX/CH4 liquid rocket engines. It is numerically studied with the AVBP solver from CERFACS, comparing two combustion models, either based on a beta-pdf equilibrium chemistry model or on reduced finite-rate chemistry. Both models lead to similar stable flame shapes, but locally higher temperatures and a shorter flame length are found with finite-rate chemistry. Phase-locked averages show that a pulsated inlet induces periodic oscillations of the heat release rate, which are however significant only at the lowest frequency.

1. Introduction

In the competitive sector of space launchers, methane is currently proposed to replace hydrogen in Liquid Rocket Engines (LRE) for operating cost reduction. Methane oxycombustion at high pressure and in subcritical or transcritical conditions raises however a number of questions that are not fully answered and require further investigation.[14] In particular, the slower oxidation chemistry of methane results in longer flames, which may also be more prone to instabilities.[9] As the extreme conditions of LRE make experiments challenging, the use of numerical simulation is essential for the understanding of the physical mechanisms at play. Among the various modelling approaches, the Large Eddy Simulation (LES) has become a standard for the study of turbulent reacting flows, and has been successfully applied to LRE in stable or transient conditions.[8,15,16,18,19] The description of chemical kinetics may be based on the infinitely fast chemistry assumption, which is well suited for hydrogen oxycombustion.[7] However, to take into account finite-rate chemistry effects which may be important for methane flames, an accurate and cost-effective model must be included. Fully detailed mechanisms are available, but their very high number of species and reactions does not allow their use in 3D LES. On the other hand, one or two-steps global schemes do not reproduce sufficient details on the flame structure. An intermediate approach is to use reduced chemistry, which optimizes the tradeoff between accuracy and complexity. In the design of LREs, much efforts are devoted to the control of thermo-acoustic instabilities which may be very detrimental to the engine operation and even lead to its destruction.[3] Although these phenomena have been extensively studied in hydrogen LREs, a different behavior is expected when methane is used. Numerical studies of flame-acoustic interaction using LES have been recently undertaken under various forced modulations[5,6,12] showing large flame induced motions depending on the modulation characteristics.

In this paper, the HF10 test case defined by the REST (Rocket Engine Stability Initiative) working group as a typical injection element of LOX/CH4 liquid rocket engines, is numerically studied. The LES approach is used and two different chemistry descriptions, either based on infinitely fast or finite-rate chemistry for comparison purposes. Thermo-acoustics are then studied via the computation of the response of the flame to mass flow rate pulsation for various pulsating frequencies.

2. Governing equations, models and numerics

The compressible unstructured solver AVBP[11,17] developed by CERFACS is used for this study. Details about the numerical strategy and the thermodynamic modeling for real-gas flows can be found in Schmitt.[15] It relies on a Taylor-Galerkin weighted residual central distribution scheme, called TTGC, third-order in time and space.[2] The subgrid-scale (SGS) stress tensor is computed with the WALE model.[13]

DOI: 10.13009/EUCASS2022-4460

Two strategies are considered in this study for the modeling of the chemical conversion. An infinitely fast chemistry model,[15] referred as IFCM, is used for all the cases. This model accounts for the following species: CH4, O2 , H2O, OH, H2, CO2 and CO in order to properly calculate the burnt gas temperature. Equilibrium reference mass fractions are tabulated in terms of the mixture fraction and its variance, both computed via transport equations in the simulations. The species source terms are then computed following the method described in Schmitt.[15]

To investigate the impact of finite-rate chemistry, an Arrhenius-based chemical scheme is also considered for the calculation of the reference case, i.e., without inlet modulation. In this approach, all chemical species of the scheme are computed via their transport equation, including an Arrhenius chemical source term. To make the 3D LES affordable, the concept of Analytically Reduced Chemistry (ARC)[4] is used to decrease the number of species and reactions, while keeping the required accuracy for selected target quantities. In addition, the Quasi Steady State Assumption (QSSA)[10] applied to the very fast species lowers the numerical stiffness of chemistry. A major advantage of ARC is to keep the most important reaction pathways, allowing to study detailed chemical effects. An ARC for methane oxycombustion at high pressure has been recently derived in[1] and is used here. It contains 14 species, 4 QSS species, and 68 reactions, and has been validated in various one-dimensional stained diffusion flame cases.

2.1 Computational domain and simulated cases

The computational domain is shown in Fig. 1 and follows the guidelines of the REST HF-10 test case. It consists in a coaxial injector fed with liquid oxygen in the center and gaseous methane in the outer. Injection temperatures are set to 100 K for oxygen and 231 K for methane and mass flow rates are 0.46 kg/s for oxygen and 0.136 kg/s for methane. All the solid boundaries are treated as adiabatic walls. Wall-laws are used at the injector walls to properly represent the boundary layer. Oxygen and methane are injected using non-reflecting boundary conditions with mass flow rates and temperatures imposed, with an amount of 5% of turbulence, while pressure is imposed at outlet (100 bar). The mesh used for all the simulations comprises 2 million nodes and is discussed in Sec. 4.

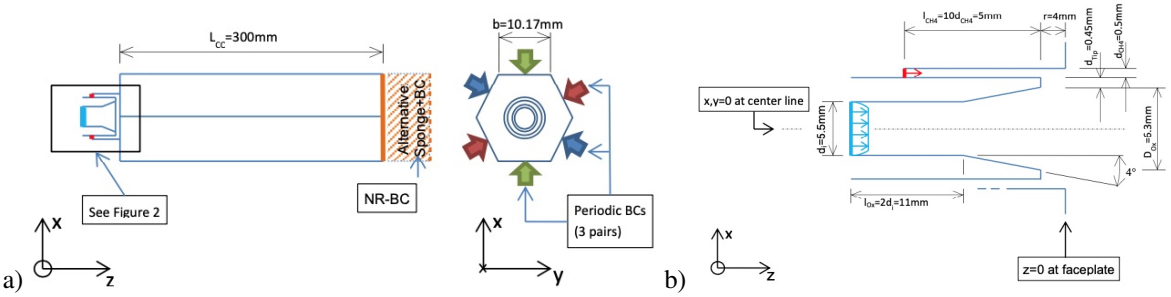

Figure 1: (a) Sketch of the full computational domain. (b) Coaxial injector.

The simulated cases are listed in Tab. 1. Two non-modulated cases (NM) are first considered. Case NM-IFCM assumes a fast chemistry coupled with a beta-pdf,[15] while in case NM-ARC an ARC is directly resolved on the grid. Cases OM correspond to oxidizer-modulated cases, with an amplitude of modulation equal to 10% of the mass flow rate. Two modulation frequencies are considered : 1 kHz and 5 kHz. For the last case, referred as FM, the fuel stream is modulated, with an amplitude of 10% of the mass flow rate and a frequency of 5 kHz. All the cases are averaged over 10 ms, corresponding to 50 periods of modulation for cases OM-5kHz and FM-5kHz and 10 periods for case OM-1kHz. The computational cost for 10 ms of physical time is 50 kh for NM-IFCM and 150 kh for NM-ARC.

Case	Mod. amp. O_2	Mod. amp. CH_4	Mod. freq.	Combustion model
NM-IFCM	-	-	-	Chemical equilibrium + β-pdf
NM-ARC	-	-	-	Analytically reduced chemistry (ARC)
OM-1kHz	10 %	0	1 kHz	Chemical equilibrium + β-pdf
OM-5kHz	10 %	0	5 kHz	Chemical equilibrium + β-pdf
FM-5kHz	0	10 %	5 kHz	Chemical equilibrium + β-pdf

Table 1: List of the simulated cases. “NM”, “OM” and “FM” stand for Non-, Oxidizer- and Fuel-Modulated, respectively.

DOI: 10.13009/EUCASS2022-4460

3. Statistical convergence

The impact of the averaging time for case NM-IFCM is shown with longitudinal profiles of mean heat release rate per unit length and of cross-averaged temperature, oxygen mass fraction and axial velocity on Fig. 2 for two averaging times: 4 ms and 8 ms. The two curves are very close to each other, suggesting that statistical convergence has been reached for mean quantities. Similar results are obtained for the mean quantities of the modulated cases, but are not shown here for the sake of brevety.

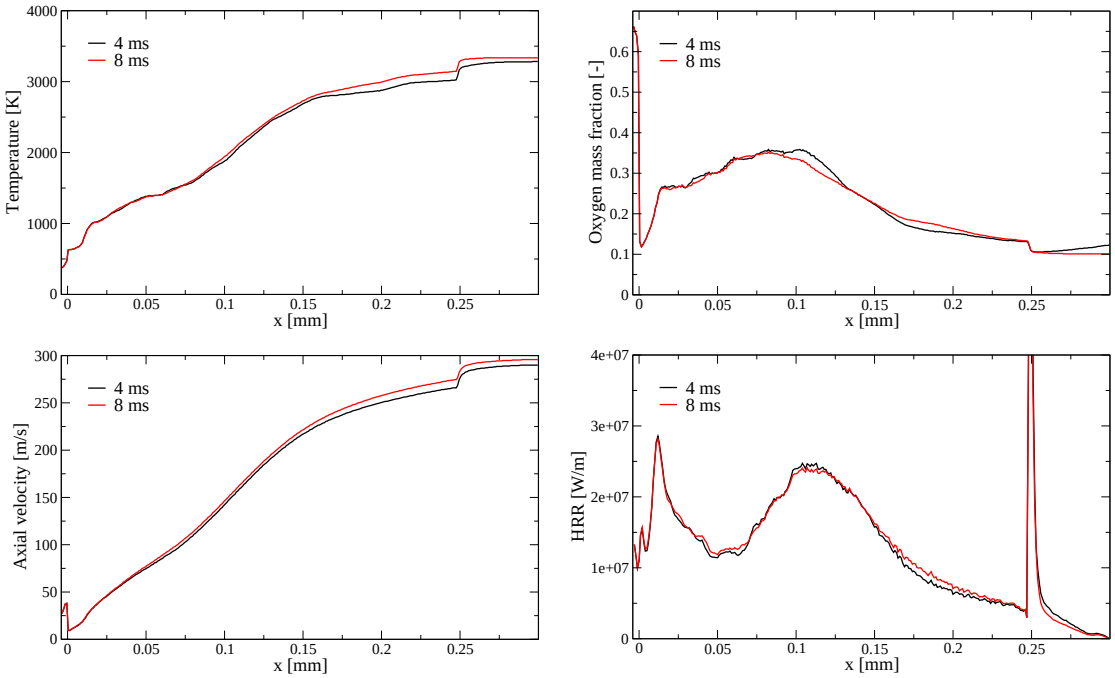

Figure 2: Longitudinal profiles for case NM-IFCM at t=4 ms and t=8 ms .

4. Impact of the mesh resolution

4.1 Meshes

Three different grid resolutions are compared for case NM-IFCM to assess the influence of the grid resolution of the simulation results. An adaptative mesh refinement technique is applied in this work. The grid is refined in regions where the flow is poorly resolved, using the Laplacian of the velocity, heat release rate and sound speed, computed from averaged solutions. Three meshes are considered. The reference one is M0. Meshes M1 and M2 correspond to one and two iterations of refinement, respectively. Longitudinal slices of the three grids in the near injector region are shown in Fig. 3. The grids are strongly refined in the recessed region and immediately at the injector exit. Details on the meshes and their respective computational costs are given in Tab. 2.

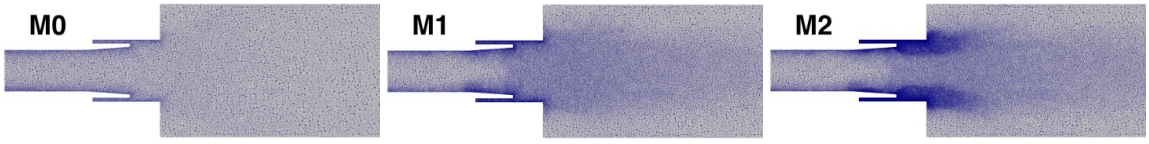

Figure 3: Longitudinal slices along the z axis with x-normal of the three meshes M0, M1 and M2.

DOI: 10.13009/EUCASS2022-4460

Mesh	Nb of cells	Nb of points	CPU cost for 10 ms [kh]
M0	3.7 10^6	0.7 10^6	7
M1	11.5 10^6	2.0 10^6	50
M2	48.1 10^6	8.3 10^6	450

Table 2: Details of the 3 meshes used for the grid convergence study with NM-IFCM case. Simulations are performed using AMD Epyc processors @2,6 GHz.

4.2 influence of the grid resolution

The three grids are compared for the case NM-IFCM. Longitudinal slices of mean oxygen mass fraction, temperature, heat release rate and axial velocity are shown in Fig. 4. Flame shapes are similar for the three meshes, with qualitatively identical flame lengths (based on the oxygen mass fraction field for exemple) and flow variable distributions. However, differences are noticeable in the recess region and at the injector exit, especially on the velocity and heat release rate, both being larger with the coarser mesh compared with the two others.

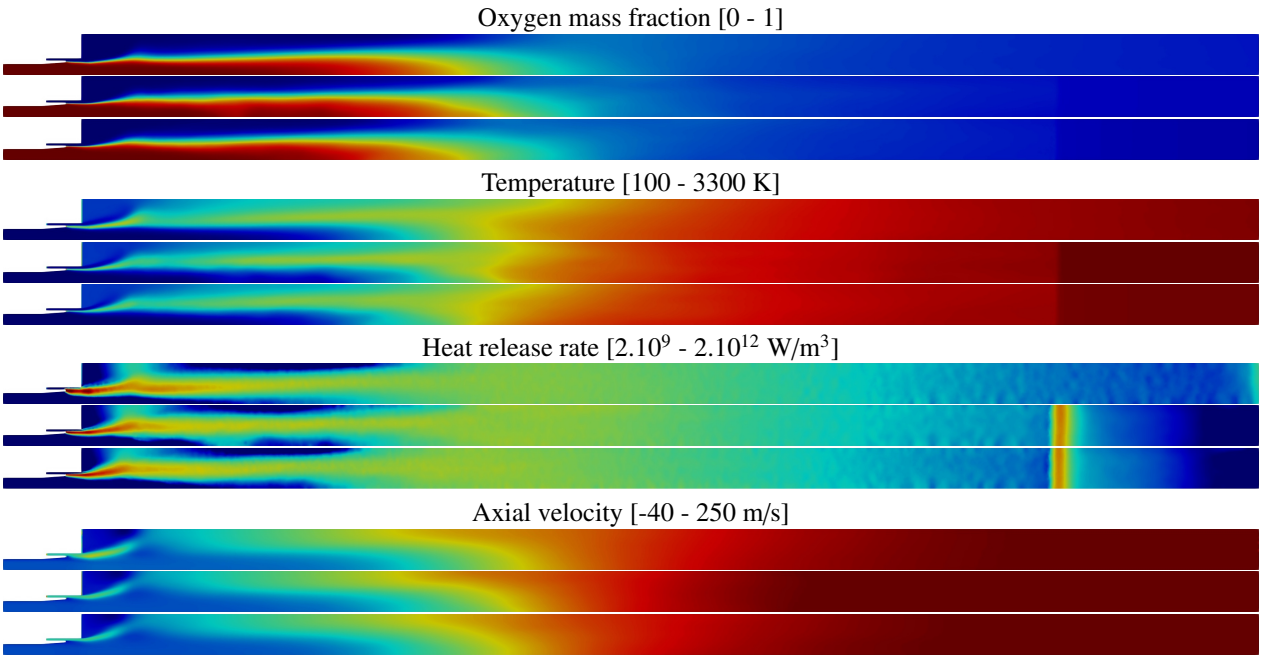

Figure 4: Longitudinal slices (top half) of mean oxygen mass fraction, temperature and heat release rate for the 3 meshes M0 (top), M1 (middle) and M2 (bottom). The huge increase of heat release rate at the end of the domain are provoked by an exit sponge layer.

For a more quantitative comparison, radial profiles of mean temperature, heat release rate and axial velocity are plotted in Figs. 5 to 7. At z=0, mesh M0 strongly departs from the two other grids: the heat release rate, temperature and consequently axial velocity are overestimated. Further downstream, the three grids show close results. Meshes M1 and M2 are in good agreement at all locations and thus M1 will be used for the rest of the study.

DOI: 10.13009/EUCASS2022-4460

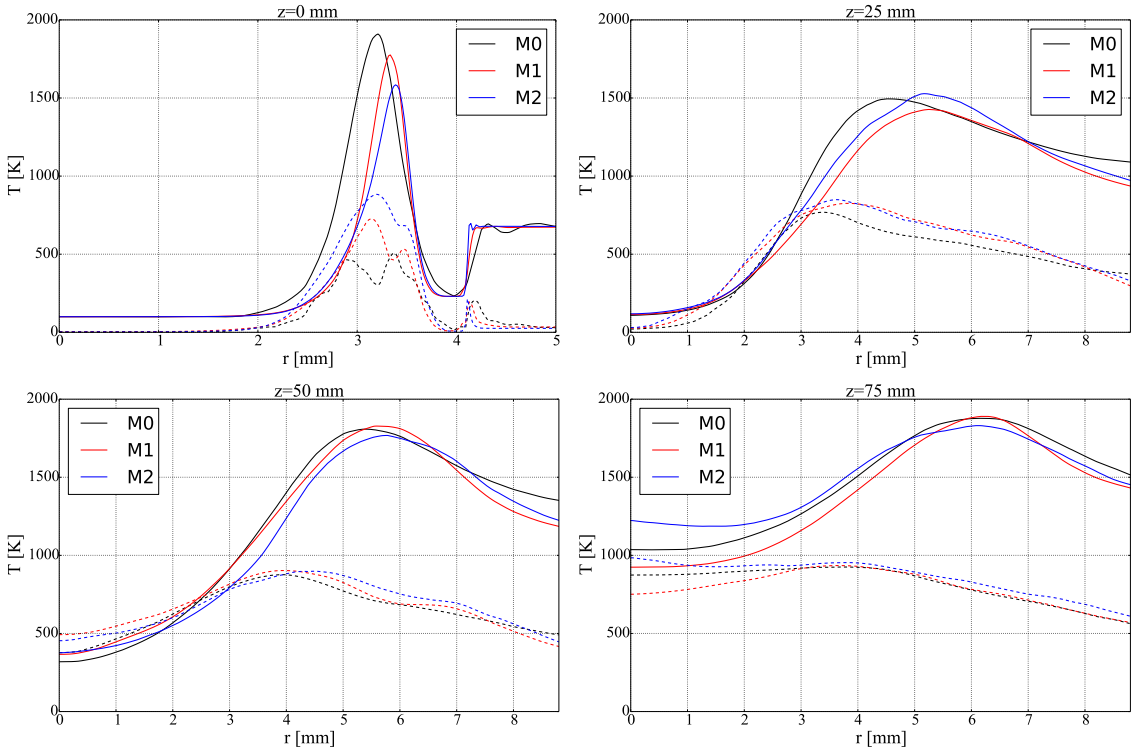

Figure 5: Radial profiles of temperature at different axial positions for meshes M0, M1 and M2. − mean profiles, −− rms profiles.

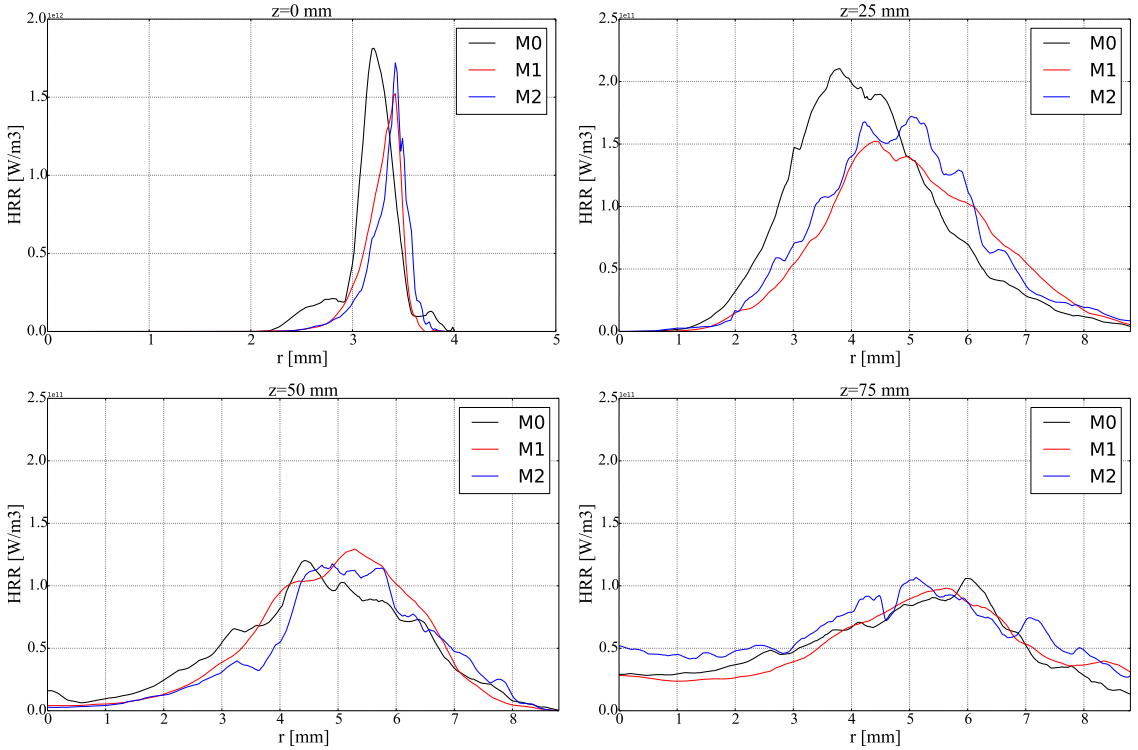

Figure 6: Radial profiles of heat release rate (HRR) at different axial positions for meshes M0, M1 and M2.

DOI: 10.13009/EUCASS2022-4460

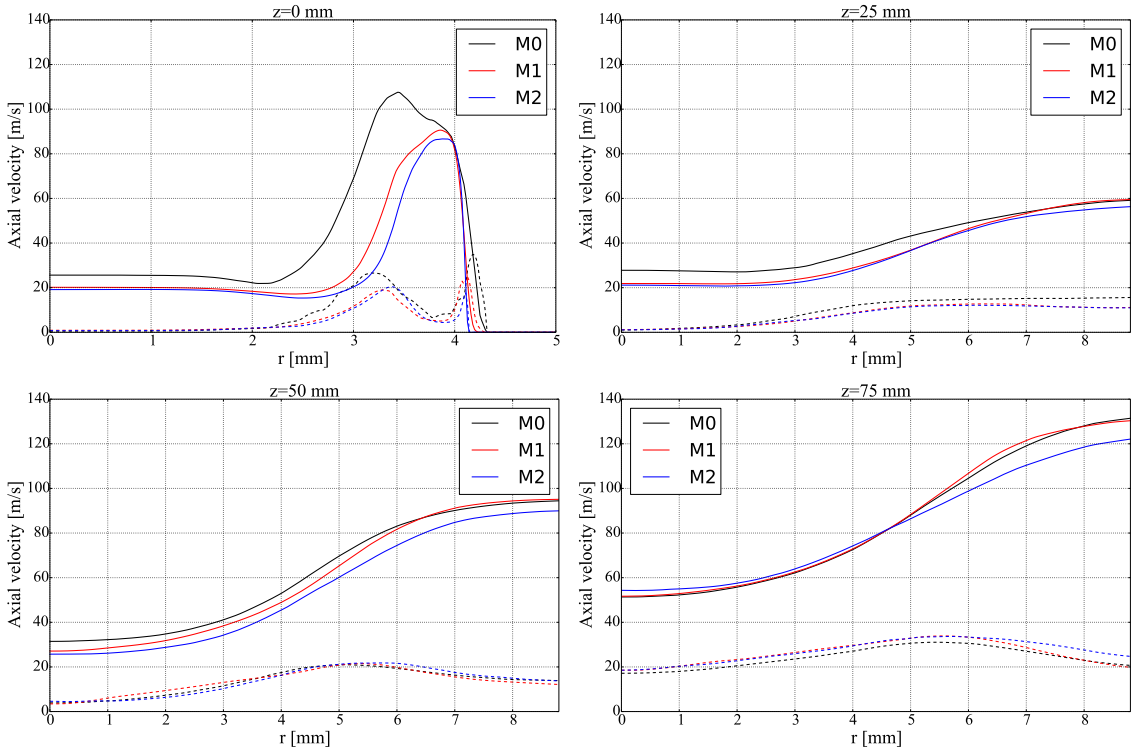

Figure 7: Radial profiles of axial velocity at different axial positions for meshes M0, M1 and M2. − mean profiles, −− rms profiles.

5. Mean results

Mean results for all the simulated cases are presented in this section. First, cases NM-IFCM and NM-ARC are compared in Sec. 5.1. Mean results for cases NM-IFCM, FM and OM are then shown in Sec. 5.2.

5.1 Comparison between NM-IFCM and NM-ARC

Mean temperature and heat release rate for cases NM-IFCM et NM-ARC are compared using longitudinal slices in Fig. 8. The overall shape of the flame is similar in both cases, indicating a similar turbulent consumption rate. However the maximum average temperature and heat release rate are higher in case NM-ARC in the first part of the chamber. This is attributed to the filtering induced by the use of a beta-pdf in the IFCM approach, while the direct integration of ARC does not involve such filtering in the current implementation. Combining the direct integration of ARC with explicit filtering may improve these results and is an on-going work.

The previous observations are in line with the longitudinal profiles shown in Fig. 9. Up to z=50mm, the temperature increases more quickly with ARC than with IFCM, then the slopes become closer until reaching a plateau around the same value. This impacts the axial velocity profile which stabillizes faster with ARC. The profiles of oxygen mass fraction also differ, showing a faster consumption with ARC in the first zone up to z=50mm and then a similar slope. Note that with ARC the oxygen mass fraction decreases below the exit equilibrium value before increasing again: this may be an effect of the semi-detailed ARC. Finally the heat release rate profiles are relatively similar, consistent with the similar flame shape.

Finally scatter plots of temperature and major species for the two simulations are provided in Fig. 10. The two scatter plots on the top are obtained from instantaneous solutions, whereas the two others are from averaged solutions. Not surprisingly, the structure of a diffusion flame is clearly recovered. As already observed from the mean fields, the IFCM results are more scattered in both the instantaneous and averaged solutions. The ARC instantaneous flame structure stays close to a strained laminar flame at a strain rate which does not strongly vary, whereas the beta-pdf introduces more variation in the IFCM case. The averaged solution shows more scattering in both cases, due to the turbulent flame motion at the resolved scale.

To evaluate the impact of the mesh on the direct integration of ARC, the NM-ARC case was also run on mesh

DOI: 10.13009/EUCASS2022-4460

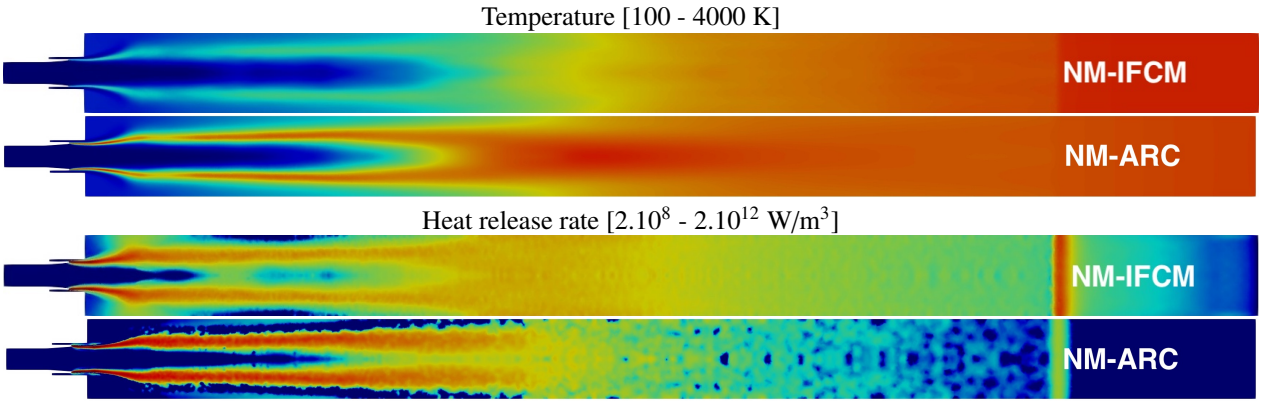

Figure 8: Longitudinal slices of mean temperature and heat release rate for cases NM-IFCM and NM-ARC.

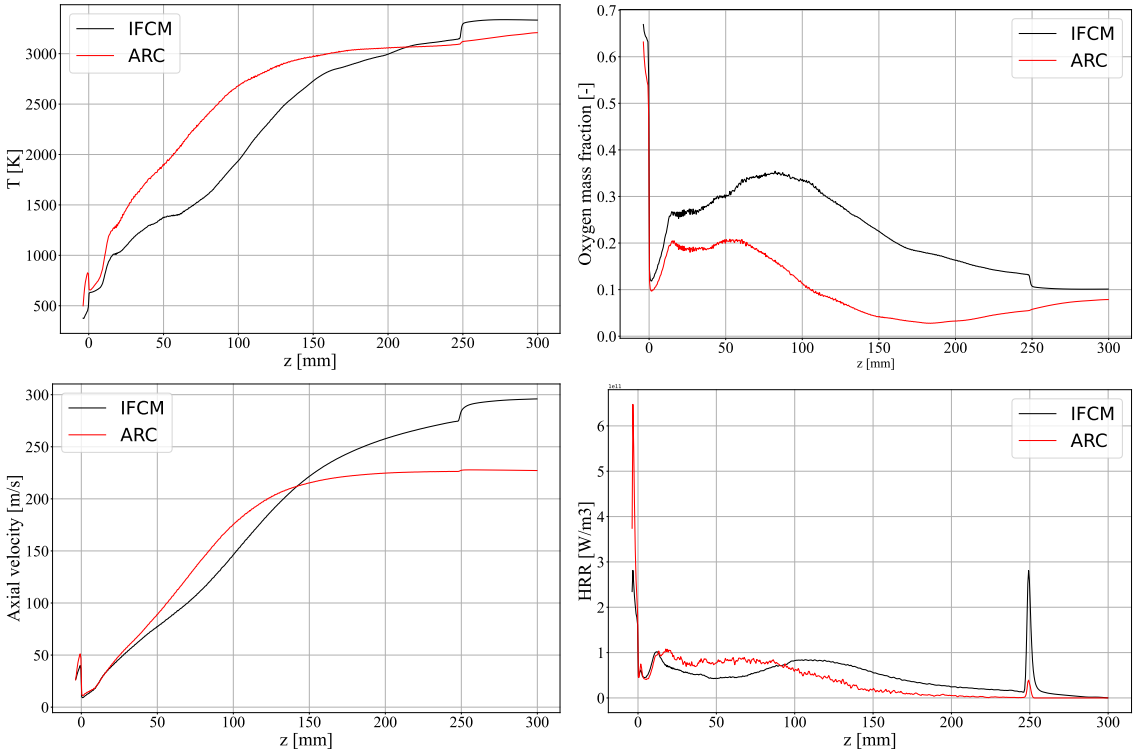

Figure 9: Longitudinal profiles of cross-averaged temperature, oxygen mass fraction, axial velocity and heat release rate for cases NM-IFCM and NM-ARC.

M2. The high computational cost did not allow to reach convergence yet and only instantaneous temperature fields are shown in Fig. 11. It seems that the temperature field comes closer to the IFCM solution when the mesh is refined, as a consequence of the lower artificial thickening of the flame by the mesh.

DOI: 10.13009/EUCASS2022-4460

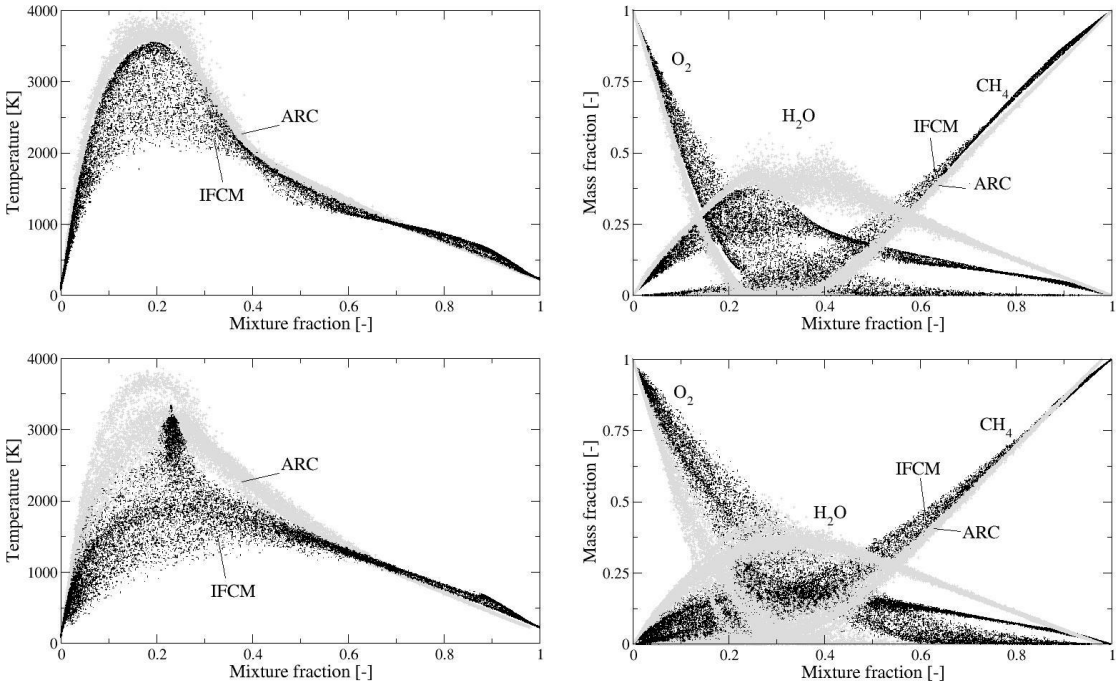

Figure 10: Scatter plots of temperature and species mass fractions in terms of the mixture fraction Z. Top: instantaneous solutions ; Bottom: average solutions.

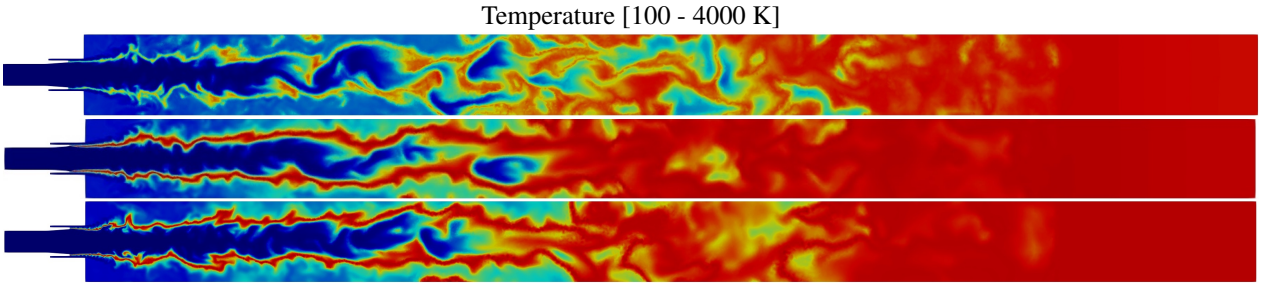

Figure 11: Longitudinal slices of instantaneous temperature for cases NM-IFCM and NM-ARC. Top: NM-IFCM, middle: NM-ARC on mesh M1, bottom: NM-ARC on mesh M2.

DOI: 10.13009/EUCASS2022-4460

5.2 Comparison between NM, OM and FM with IFCM

Longitudinal slices in the z-y plane are shown in Fig. 12 for the temperature and heat release rate fields. All the 4 cases show very close results, with negligible differences. This is confirmed with the longitudinal profiles of cross-averaged variables plotted in Fig. 13. The flame NM seems however slightly longer than the 3 others, but the difference remains very small and could be due to statistical limitations. Additional radial profiles of temperature and heat release rate are plotted in Figs. 14 and 15. The larger departure is on the heat release rate, lower in the region 25 mm < z < 100 mm for case NM. In general, for the cases considered here, the modulation seems to have a negligible impact on the mean flame topology.

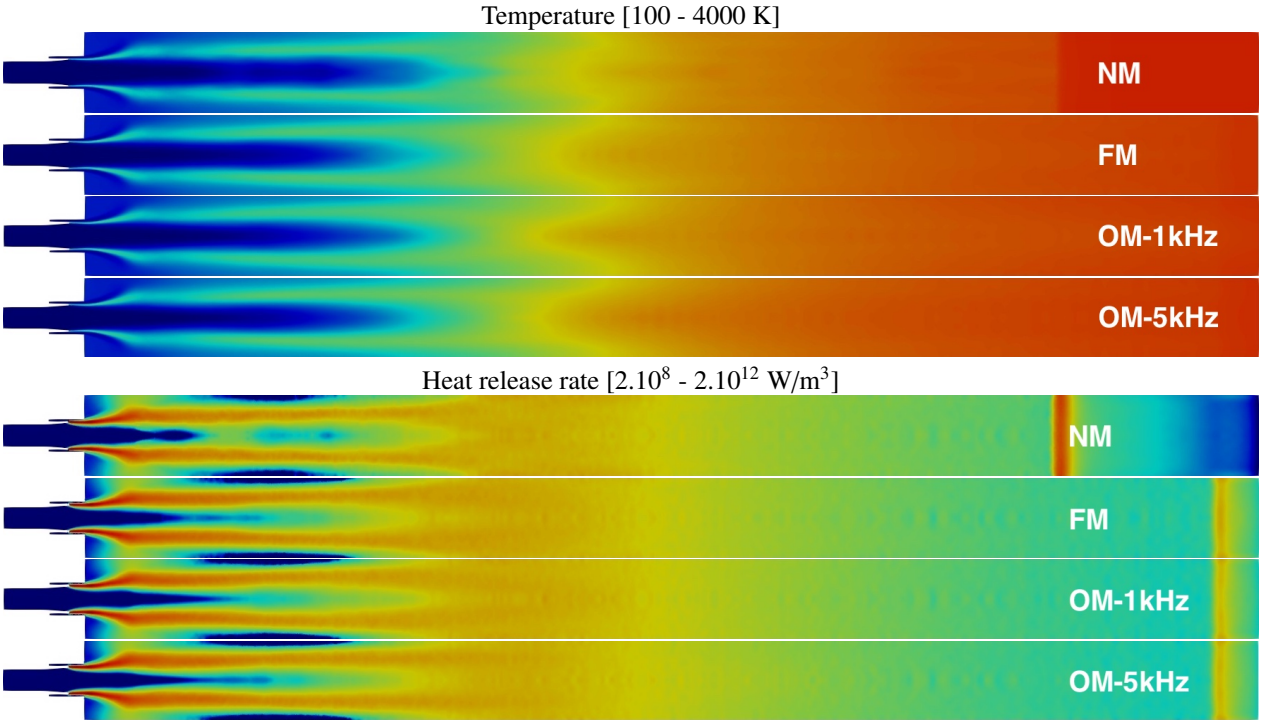

Figure 12: Longitudinal slices of mean temperature and mean heat release rate for cases NM, FM and OM.

DOI: 10.13009/EUCASS2022-4460

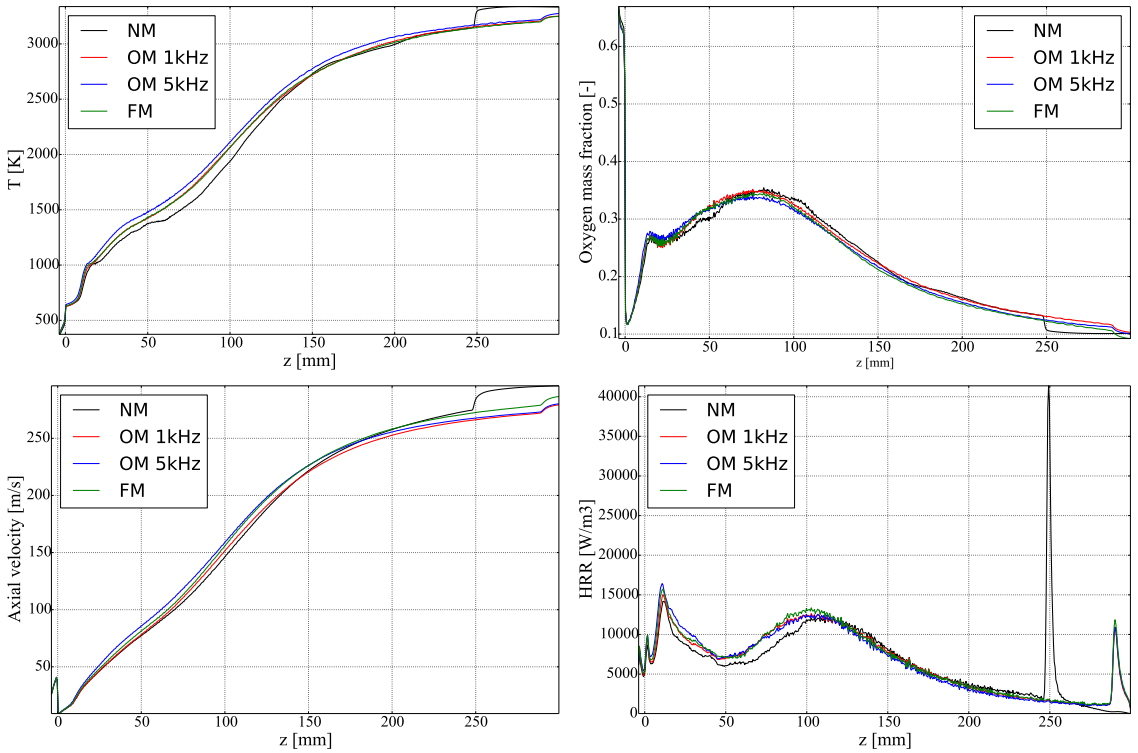

Figure 13: Longitudinal profiles of cross-averaged temperature, oxygen mass fraction, axial velocity and heat release rate for cases NM, FM and OM.

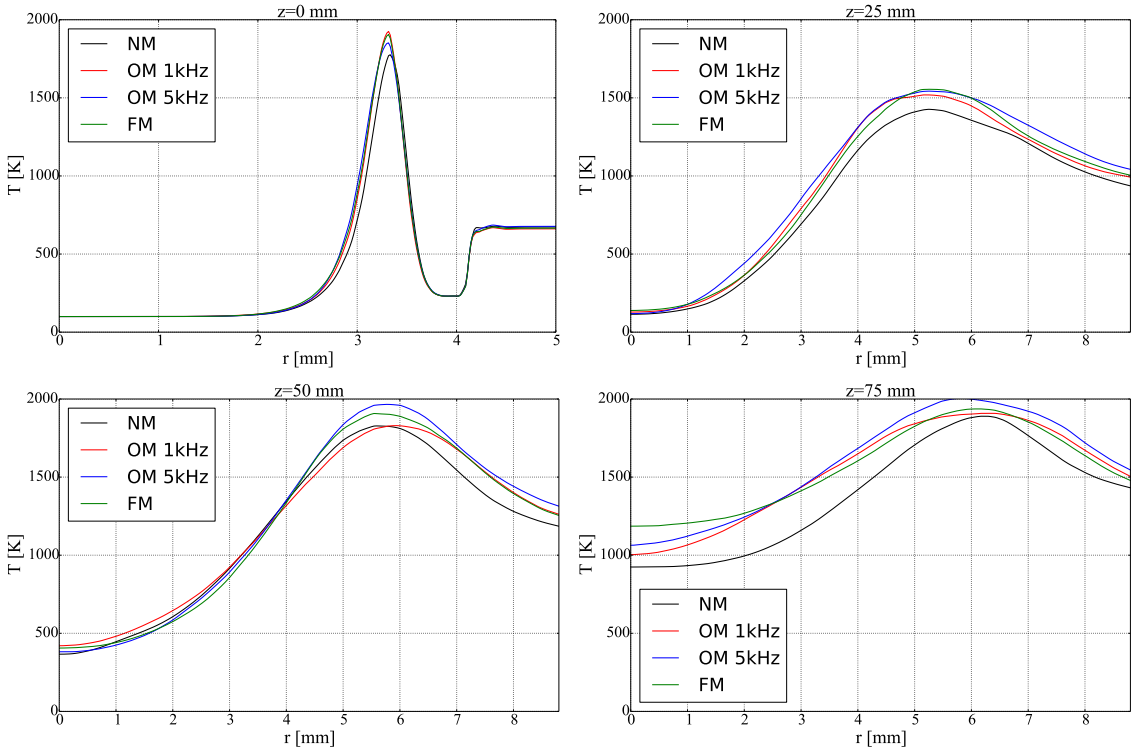

Figure 14: Radial profiles of mean temperature at different axial positions for cases NM, FM and OM.

DOI: 10.13009/EUCASS2022-4460

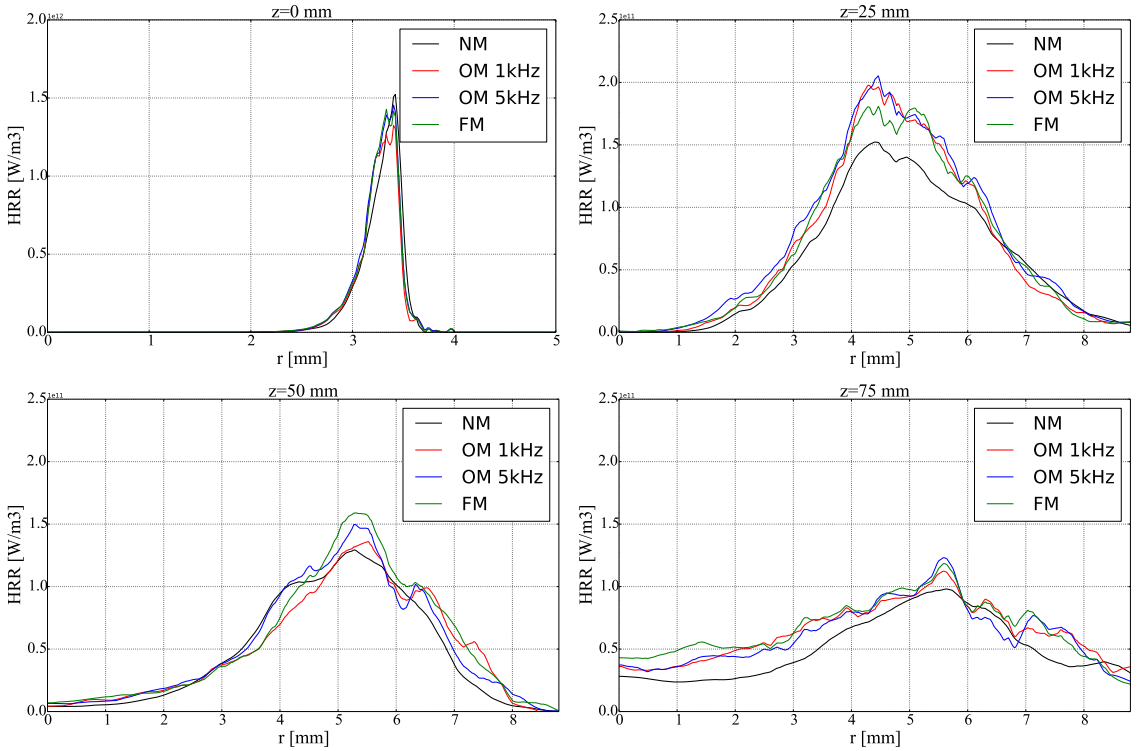

Figure 15: Radial profiles of mean heat release rate (HRR) at different axial positions for cases NM, FM and OM.

6. Phase-averaged results

The modulated simulations are now presented in terms of phase-averaged quantities. First, longitudinal slices are proposed in Sec. 6.1. Then, phase-averaged fluctuations fields are discussed in Sec. 6.2. Finally, the integrated flame response is given in Sec. 6.3.

6.1 Longitudinal slices (x-normal)

Slices of phase-averaged temperature and heat release rate are shown in Fig. 16 and 17 for $\phi = 0$ and $\phi = \pi$, ϕ being the phase of the modulation (equal to 0 when the modulated mass flow rate is minimum at inlets). All the cases show a corrugated inner jet, either directly provoked by the inner stream modulation or indirectly by the modulation of the annular jet. The wave length of the modulation roughly results from the central velocity and the modulation frequency. The heat release rate is importantly modulated at the injector exit for all the cases and at the end of the flame for case OM-1kHz.

6.2 Phase-averaged fluctuations

To properly identify the fluctuations induced by the modulations, it is convenient to look at phase-averaged fluctuations. For the heat release rate, it is defined as HRR'(ϕ)=HRR(ϕ)-<HRR>, <> indicating a temporal averaging procedure. Results are shown in Fig. 18 for all the modulated cases. Most heat release rate fluctuations induced by the inlet modulation are confined just at the injector exit for the two cases at 5 kHz. On the contrary, the case at 1kHz shows longer wave oscillations up to the middle of the domain. It is also interesting to notice that high frequency modulations produce a short wave length pattern of positive and negative contributions, which are expected to cancel each other once integrated over the flame length.

DOI: 10.13009/EUCASS2022-4460

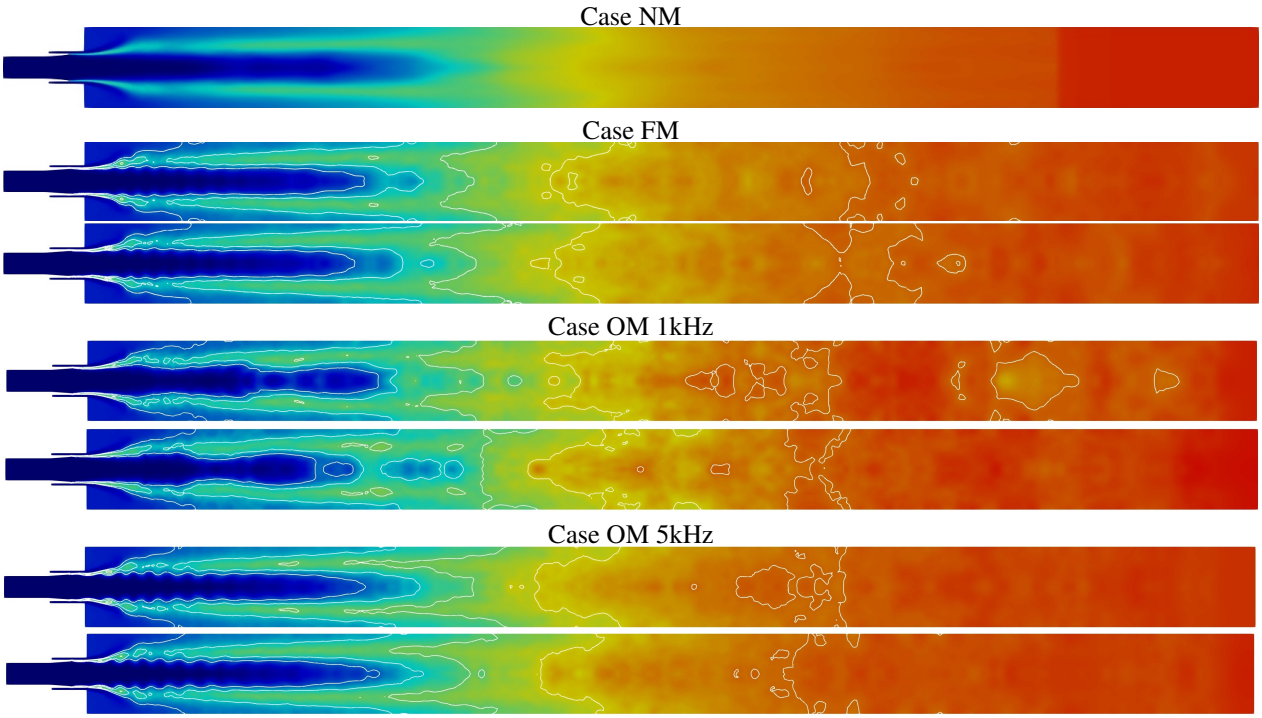

Figure 16: Longitudinal slices of phase-averaged temperature (between 100 and 4000 K) for $\phi = 0$ and $\phi = \pi$.

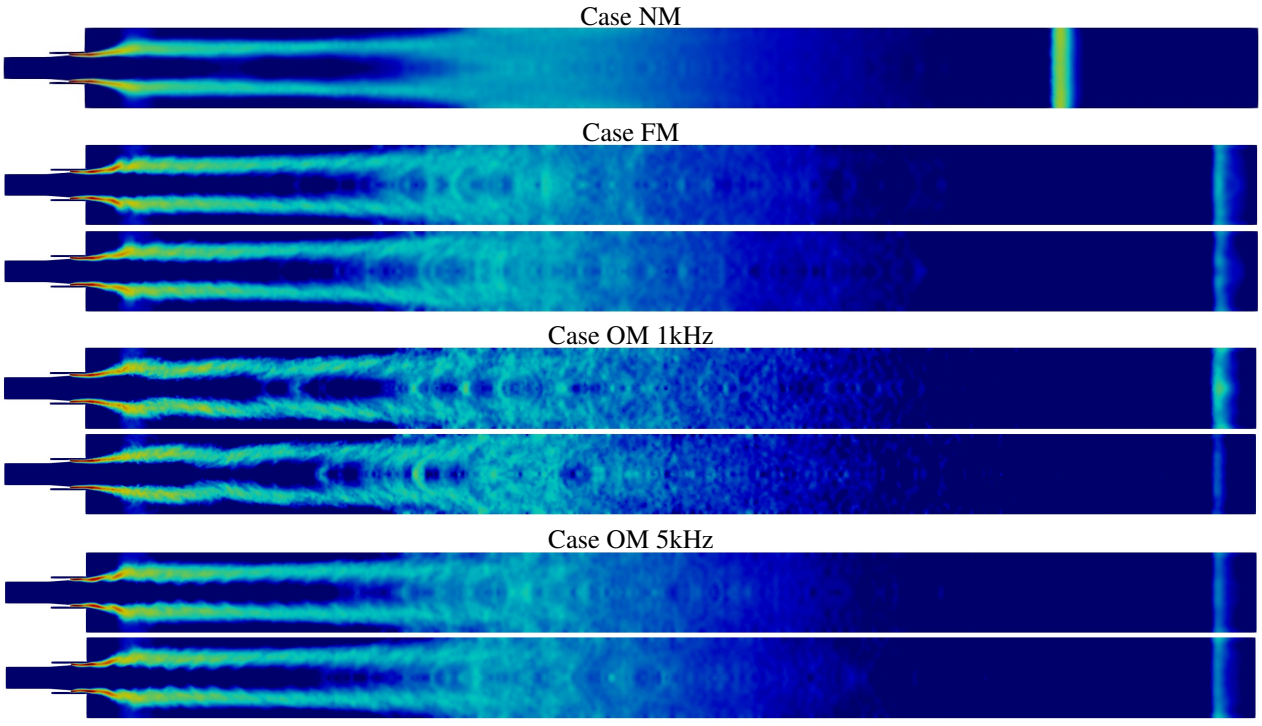

Figure 17: Longitudinal slices of phase-averaged heat release rate (between 2.10^{10} W/m^3 and 2.10^{12} W/m^3) for $\phi = 0$ and $\phi = \pi$.

6.3 Integrated flame response

The heat release rate fluctuations over one period of modulation are integrated over the whole domain (excluding the sponge layer region at the end of the chamber). Inlet mass flow rate modulations are shown in Fig. 19a and follows

DOI: 10.13009/EUCASS2022-4460

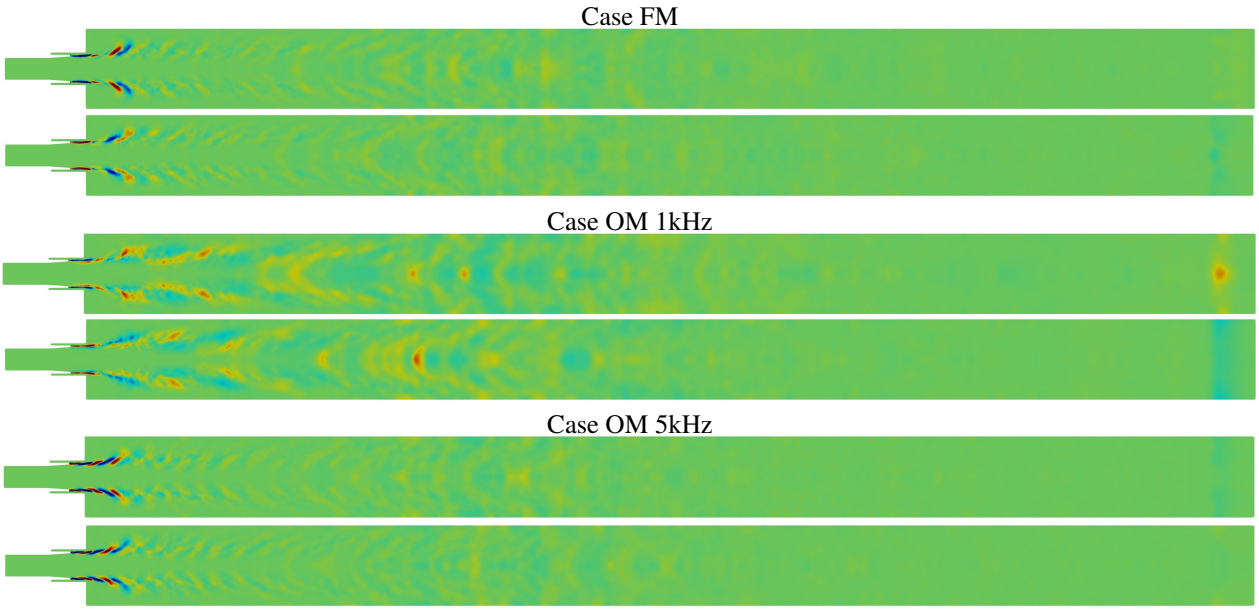

Figure 18: Longitudinal slices of phase-averaged heat release rate fluctuations (between -2.10^{11} W/m^3 and 2.10^{11} W/m^3) for $\phi = 0$ and $\phi = \pi$.

the test case description: $\phi = 0$ is defined at the minimum mass flow rate at inlet. The flame response is plotted in Fig. 19b. To ease the reading, the results are multiplied by 10 on the figure, roughly accounting for the modulation amplitude (*i.e.* 0.1) in order to mimic a gain. The two cases at 5 kHz, namely FM and OM-5kHz, show very small amplitude oscillations, with a gain lower than 0.03. On the contrary, a gain close to 0.25 is noticed for case OM-1kHz. This results should however be taken with care: a strong sensitivity to the averaging time is noticed and results with only 20 periods of modulation might not be properly converged. However, this result indicates that case OM-1kHz is a convenient case for solver comparison and an additional lower modulation frequency should be considered for case FM in order to produce an effective flame response.

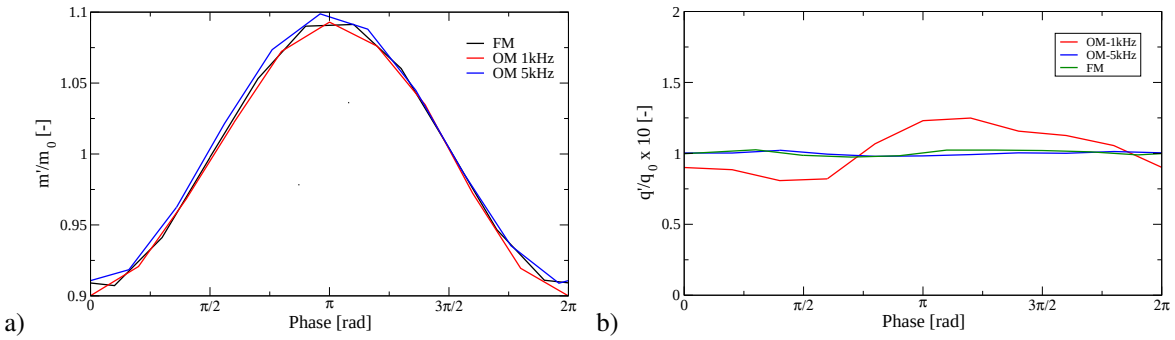

Figure 19: a) Inlets mass flow rate (oxygen for OM cases and methane for FM case) over a period. b) Integrated heat release rate fluctuations q' normalized by the averaged value q_0 over a period. The amplitude is multiplied by 10 to account for the amplitude of modulation (0.1) and roughly represents a gain.

7. Conclusions

This work was realized in the framework of the REST (Rocket Engine Stability Initiative) working group on combustion instabilities in liquid rocket engines. The HF-10 test case is representative of a typical injection element from a liquid rocket engine, subject to pulsating mass flow rates at the inlet. The test comprises 3 sub-cases. In the first case, the outer flow (CH4) is pulsated at 5kHz. The second case consists in modulating the inner flow (O2) at 1kHz and in the third

DOI: 10.13009/EUCASS2022-4460

case the inner flow is pulsated at 5kHz. The HF-10 test case was simulated using the AVBP solver from CERFACS. The numerical approach relies on real-gas thermodynamics based on the SRK equation of state. Two combustion models are investigated: a beta-pdf based equilibrium chemistry model (IFCM) and an Arrhenius based finite-rate chemistry model, with an ARC scheme specifically derived for the present cases.

The computed flame reaches about one third of the combustion chamber length for the isoline at 1500K. The flame expands quickly after the injection plane, and large scale intermittencies are observed. A mesh convergence is performed with the IFCM combustion model. It is found that after one iteration of localized refinement, the results do not show noticeable sensitivity to the grid resolution.

Comparison between IFCM and ARC chemical modeling indicates that the two chemical approaches lead to similar flame topologies. The finite-rate chemistry flame structure confirms that combustion occurs in a pure diffusion flame regime in this adiabatic configuration. However, in its current implementation, the direct integration of ARC requires a finer grid resolution in the flame front than the β-pdf model to better take into account the flame-turbulence interaction. As a consequence, for the grid resolution retained in this study, ARC produces a higher temperature field than IFCM.

Inlet pulsations do not significantly change the flame topology, both for OM and FM cases, when compared with the non-modulated case. However, phase-locked averages show induced periodic oscillations of the heat release rate along the flame. For the high-frequency cases at 5 kHz, these oscillations cancel along the flame length and the final contribution after integrating the heat release rate over the whole flame length is limited (the gain is lower than 0.03). On the contrary, the case OM at 1 kHz shows an important modulation of the flame heat release rate, close to a gain of 0.25. However, it is also found that with the number of modulation periods retained in this test case (10 in the recommendations - 20 used in this work), the phase averaged flame response may not be properly converged with possible errors on both the gain and the phase. These results suggest that case OM 1kHz should be averaged over a longer physical time and that a lower frequency of modulation should be envisaged for case FM in the future HF-10 test case description.

Acknowledgements

This work was granted access to the HPC resources of TGCC (CEA), IDRIS and CINES made available by GENCI (Grand Equipement National de Calcul Intensif) under the allocation A0102B06176. A part of this work was performed using HPC resources from the mésocentre computing center of Ecole CentraleSupélec and Ecole Normale Supérieure Paris-Saclay supported by CNRS and Région Ile-de-France.

References

[1] S. Blanchard, Q. Cazères, and B. Cuenot. Chemical modeling for methane oxy-combustion in liquid rocket engines. *Acta Astronautica*, 190:98–111, 2022.

[2] O. Colin and M. Rudgyard. Development of high-order Taylor-Galerkin schemes for unsteady calculations. *J. Comput. Phys.*, 162(2):338–371, 2000.

[3] F. E. C. Culick and V. Yang. Overview of Combustion Instabilities in Liquid-Propellant Rocket Engines. In V. Yang and W. E. Anderson, editors, *Liquid Rocket Engine Combustion Instability*, volume 169, pages 3–37. Washington, DC: AIAA, Inc, 1995.

[4] J. F. Griffiths. Reduced kinetic models and their application to practical combustion systems. *Progress in Energy and Combustion Science*, 21(1):25–107, 1995.

[5] L. Hakim, A. Ruiz, T. Schmitt, M. Boileau, G. Staffelbach, S. Ducruix, B. Cuenot, and S. Candel. Large eddy simulations of multiple transcritical coaxial flames submitted to a high-frequency transverse acoustic modulation. *Proceedings of the Combustion Institute*, 35(2):1461–1468, 2015.

[6] L. Hakim, T. Schmitt, S. Ducruix, and S. Candel. Dynamics of a transcritical coaxial flame under a high-frequency transverse acoustic forcing: Influence of the modulation frequency on the flame response. *Combustion and Flame*, 162(10):3482–3502, 2015.

[7] B. Ivancic and W. Mayer. Time and length scales of mixing and combustion processes in high-pressure LOx/GH_2 rocket combustors. *Journal of Propulsion and Power*, 18(2):247–253, 2002.

DOI: 10.13009/EUCASS2022-4460

[8] G. Lacaze, B. Cuenot, T. Poinsot, and M. Oschwald. Large eddy simulation of laser ignition and compressible reacting flow in a rocket-like configuration. *Combustion and Flame*, (6):1166–1180, 2009.

[9] Dong Li, Qi Zhang, Qiuju Ma, and Shilei Shen. Comparison of explosion characteristics between hydrogen/air and methane/air at the stoichiometric concentrations. *International Journal of Hydrogen Energy*, 40(28):8761–8768, 2015.

[10] Tianfeng Lu and Chung Law. Systematic approach to obtain analytic solutions of quasi steady state species in reduced mechanisms. *Journal of Physical Chemistry A*, 110(49):13202–13208, 2006.

[11] V. Moureau, G. Lartigue, Y. Sommerer, C. Angelberger, O. Colin, and T. Poinsot. High-order methods for DNS and LES of compressible multi-component reacting flows on fixed and moving grids. *J. of Comput. Phys.*, 202(2):710–736, 2005.

[12] Robin Nez, Thomas Schmitt, and Sébastien Ducruix. High-frequency combustion instabilities in liquid rocket engines driven by propellants flow rate oscillations. In *3AF SpacePropulsion 2018 Conference*, 2018.

[13] F. Nicoud and F. Ducros. Subgrid-scale stress modelling based on the square of the velocity gradient. *Flow, Turbulence and Combustion*, 62(3):183–200, 1999.

[14] A Preuss, D Preclik, C Mading, J Gorgen, S Soller, O Haidn, M Oschwald, W Clauss, R Arnold, and J Sender. LOX/Methane Technology Efforts for Future Liquid Rocket Engines. In *5th International Spacecraft Propulsion Conference & 2nd International Symposium on Propulsion for Space Transportation*, 2008.

[15] T. Schmitt. Large-eddy simulations of the mascotte test cases operating at supercritical pressure. *Flow, Turbulence and Combustion*, 105:159–189, 2020.

[16] T. Schmitt, Y. Méry, M. Boileau, and S. Candel. Large-eddy simulation of oxygen/methane flames under transcritical conditions. *Proc. Combust. Inst.*, 33:1383–1390, 2011.

[17] T. Schönfeld and M. Rudgyard. Steady and unsteady flows simulations using the hybrid flow solver avbp. *AIAA Journal*, 37(11):1378–1385, 1999.

[18] A Urbano, Q Douasbin, L Selle, G Staffelbach, B Cuenot, T Schmitt, S Ducruix, and S Candel. Study of flame response to transverse acoustic modes from the les of a 42-injector rocket engine. *Proceedings of the Combustion Institute*, 36(2):2633–2639, 2017.

[19] A. Urbano, L. Selle, G. Staffelbach, B. Cuenot, T. Schmitt, S. Ducruix, and S. Candel. Exploration of combustion instability triggering using large eddy simulation of a multiple injector liquid rocket engine. *Combustion and Flame*, 169:129–140, 2016.